RESEARCH ARTICLE
PLANETARY SCIENCE

Earth and Planetary Physics
2: 292–302, 2018
doi: 10.26464/epp2018027

Optimization of the Mars ionospheric radio occultation retrieval

JunYi Wang[1,2], XinAn Yue[1,2,3*], Yong Wei[1,2,3], and WeiXing Wan[1,2,3]

[1]Key Laboratory of Earth and Planetary Physics, Institute of Geology and Geophysics, Chinese Academy of Sciences, Beijing 100029, China;

[2]Institutions of Earth Science, Chinese Academy of Sciences, Beijing 100029, China;

[3]College of Earth and Planetary Sciences, University of Chinese Academy of Sciences, Beijing 100049, China

Abstract: Electron density is a key parameter to characterize Martian ionospheric structure and dynamics. Based on the ephemeris and auxiliary information derived from the Spacecraft, Planet, Instruments, C-matrix, and Events (SPICE) toolkit, we calculated the bending angle of signal path from the frequency residuals measured by the Mars Express Radio Science Experiment (MaRS) of the Mars Express (MEX) mission under the assumption of a spherically symmetric ionosphere. We stratified the ionosphere into layers and assumed a linear change of bending angle between layers, to derive profiles in radial distance of refractivity with the optimized parameters of upper integral limit of 4890 km and baseline correction boundary of 3690 km. Meanwhile, we also compared the retrieved electron density profiles between the frequency residuals of the single-frequency and differential Doppler of the dual-frequency. In total, ~640 electron density profiles of Martian ionosphere between April 2004 and April 2015 were retrieved successfully. There are 24 profiles identified manually that exhibit an additional sporadic layer occurrence below the normal two-layers. We also found that the peak altitude of this layer increases with the main peak altitude.

Keywords: Mars; ionosphere; radio occultation; electron density

Citation: Wang J. Y., Yue X. A., Wei Y., and Wan W. X. (2018). Optimization of the Mars ionospheric radio occultation retrieval. *Earth Planet. Phys.*, *2*(4), 292–302. http://doi.org/10.26464/epp2018027

1. Introduction

Radio occultation (RO) is a remote sensing method that employs radio transmitter/receiver pairs with signal passing through a planetary atmosphere and/or ionosphere, whose information therefore can be derived from the phase delay of the radio signals. This technology was first applied in the Mariner-4 mission; the spacecraft's measuring and controlling signal was used to detect the Martian ionosphere and lower atmosphere (Kliore et al., 1965; Fjeldbo and Eshleman, 1965). Since then, the RO method has been widely used in most planetary missions due to its flexibility and highly cost-effective performance (Fjeldbo and Eshleman, 1969; Fjeldbo et al., 1970; Kliore et al., 1972; Michael et al., 1972; Lindal et al., 1979; Hinson et al., 1999; Pätzold et al., 2004; Withers et al., 2012; Haider and Mahajan, 2014; Withers et al., 2015). Our knowledge of planetary ionosphere and neutral atmosphere before 1980 s mainly came from multiple missions with RO capability (Hantsch and Bauer, 1990).

The Mars Express (MEX) was the first Mars mission of the European Space Agency (ESA). It entered into Mars' orbit on 25 December 2003 (Chicarro et al., 2004). One of its main payloads is the Mars Express Radio Science Experiment (MaRS). It started regular operation in April 2004 and employed the RO technique to sound the Martian ionosphere and neutral atmosphere with two-way tracking mode, in which the ground station transmitted an uplink radio signal (f=7.1 GHz) and received the dual-frequency downlink signals at X-Band (8.4 GHz) and S-Band (2.3 GHz), respectively. The ground network of stations, including the ESA stations in Australia and the Deep Space Network (DSN) in America, Spain, and Australia (Pätzold et al., 2016) measured the downlink radio signals with both closed- and open-loop recording modes (Pätzold et al., 2004, 2009). These data have been widely used by the community in investigations and data evaluations (Grandin et al., 2015; Marissa et al., 2016; Peter et al., 2014; Sánchezcano et al., 2012; Withers et al., 2014).

Although the Mars RO data have been widely used in the literature, its retrieval algorithm has not been studied comprehensively, especially parameter optimization (Cahoy et al., 2006; Fjeldbo et al., 1971; Withers et al., 2014; Zhang S J et al., 2011, 2015; Zou H et al., 2016). In this paper, we first outline how the frequency residuals and differential Doppler data from MaRS are utilized to determine the vertical electron density profile (EDP) of the ionosphere. Then we will determine how to choose the best parameter configuration in the data retrieval, including the baseline correction boundary, integrating upper limit, and fitting method. Given that several new Mars missions, including the Chinese 2020 Mars exploration, will be implemented in the near future (Jiang X et al., 2018), it remains great significance to continue this kind of research.

2. Data Processing Algorithm

When the spacecraft flies to the far side of Mars, its radio signal ray

Correspondence to: X. A. Yue, yuexinan@mail.iggcas.ac.cn
Received 22 MAY 2018; Accepted 27 JUN 2018.
Accepted article online 09 JUL 2018.

passes, on its way to ground tracking stations, through the Martian atmosphere and ionosphere, which enables measurement of their effects on the radio signals. Figure 1 shows typical geometry of a Mars RO event. Our research was based on the level-2 data of MaRS, which included the ground receiving time, frequency residuals, and differential Doppler processed from the original level 1a and 1b data (Pätzold et al., 2016). The ephemeris and other auxiliary information were derived from the SPICE (Spacecraft, Planet, Instruments, C-matrix, and Events) toolkit published by NASA (the National Aeronautics and Space Administration) NAIF (Navigation and Ancillary Information Facility).

Given the ephemeris second of the ground receiving time, the positions of Mars, the Earth, and the spacecraft in the equatorial geocentric coordinate system (known as J2000) could be obtained first. The signal propagation time Δt is calculated via the relationship $|\boldsymbol{R}_{\rm C}(t-\Delta t)-\boldsymbol{R}_{\rm E}(t)|=c\times\Delta t$. Then the direction vectors of Mars to Earth $\boldsymbol{R}_{\rm M-E}(t)$ and Mars to the spacecraft $\boldsymbol{R}_{\rm M-C}(t-\Delta t)$ are used to build the occultation plane, as shown in Figure 1. The plane normal vector of this coordinate system is $\boldsymbol{n}=\boldsymbol{R}_{\rm M-E}(t)\times\boldsymbol{R}_{\rm M-C}(t-\Delta t)$, and negative z axis is the direction of $\boldsymbol{R}_{\rm M-E}(t)$.

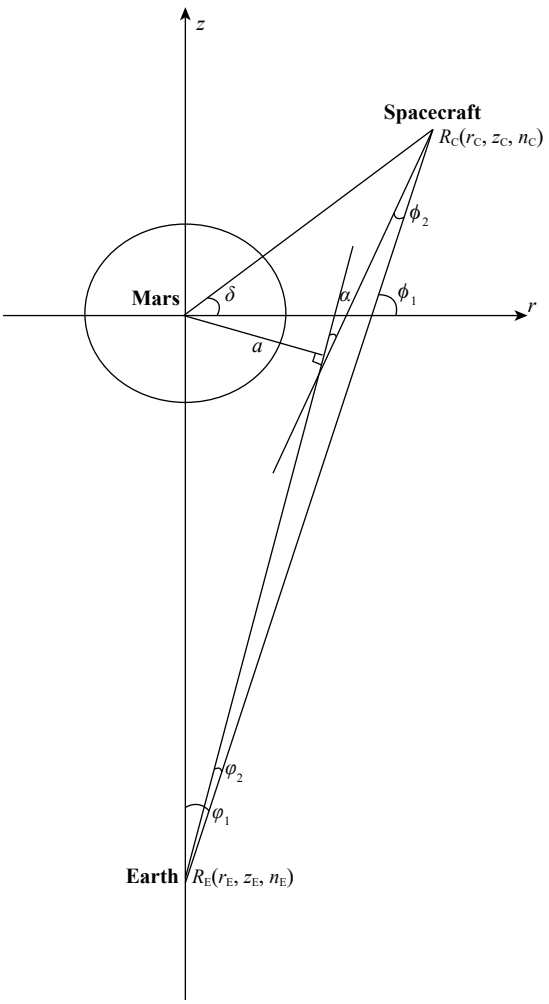

Figure 1. Demonstration of the MaRS (Mars Express Radio Science Experiment) radio occultation coordinate system (Fjeldbo et al., 1971). $R_{\rm C}(r_{\rm C}, z_{\rm C}, n_{\rm C})$, $R_{\rm E}(r_{\rm E}, z_{\rm E}, n_{\rm E})$ are respectively the positions of the spacecraft and of the Earth; δ is the angle between the direction vector of Mars to the spacecraft and the r axes; ϕ_1 is the angle between the direction vector of the Earth to the spacecraft and the r axes; ϕ_2 is the angle between the ray asymptote and the direction vector of the Earth to the spacecraft; φ_1 is the angle between the direction vector of the Earth to the spacecraft and the z axes; φ_2 is the angle between the ray asymptote and the direction vector of the Earth to the spacecraft; α is the ray bending angle; a is the impact parameter.

As is well known, any two different coordinate systems can be transformed by rotation of the three coordinate axes. The transition matrixes we used are as follows:

$$\boldsymbol{R}_X=\begin{bmatrix}1 & 0 & 0\\ 0 & \cos\beta_X & \sin\beta_X\\ 0 & -\sin\beta_X & \cos\beta_X\end{bmatrix},$$
$$\boldsymbol{R}_Y=\begin{bmatrix}\cos\beta_Y & 0 & -\sin\beta_Y\\ 0 & 1 & 0\\ \sin\beta_Y & 0 & \cos\beta_Y\end{bmatrix},$$
$$\boldsymbol{R}_Z=\begin{bmatrix}\cos\beta_Z & \sin\beta_Z & 0\\ -\sin\beta_Z & \cos\beta_Z & 0\\ 0 & 0 & 1\end{bmatrix}, \quad (1)$$

where β_X, β_Y, β_Z is the rotation angle from J2000 to occultation coordinate system in each axis, and they are defined as:

$$\beta_X=\begin{cases}90^\circ,\ C=0,\ B<0\\ -90^\circ,\ C=0,\ B>0\\ -\arctan(B/C),\ C>0\\ 180^\circ-\arctan(B/C),\ C<0\end{cases}$$
$$\beta_Y=\begin{cases}90^\circ,\ C'=0,\ A>0\\ -90^\circ,\ C'=0,\ A<0\\ \arctan(A/C),\ C'>0\\ 180^\circ+\arctan(A/C),\ C'<0\end{cases}$$
$$\beta_Z=\begin{cases}-90^\circ,\ E=0,\ D<0\\ 90^\circ,\ E=0,\ D>0\\ 180^\circ-\arctan(D/E),\ E>0\\ -\arctan(D/E),\ E<0\end{cases}$$
$$\begin{bmatrix}A\\0\\C'\end{bmatrix}=\boldsymbol{R}_X(\beta_X)\begin{bmatrix}A\\B\\C\end{bmatrix},\ \begin{bmatrix}D\\E\\0\end{bmatrix}=\boldsymbol{R}_Y(\beta_Y)\boldsymbol{R}_X(\beta_X)\boldsymbol{R}_{\rm M-E}, \quad (2)$$

in which, (A,B,C) is the direction vector in the equatorial geocentric coordinate system, $(A,0,C')$ is the direction vector after the rotation of the X axis, and $(D,E,0)$ is the direction vector after the rotation of the X and Y axes. When the above steps have been taken, the positions and velocities of the Earth and the spacecraft in the occultation plane coordinate system are obtained with the consideration of the signal propagating time delay. We can then compute the ray bending angle and the impact parameter used below.

3. Electron Density Profile Retrieval

The frequency residual of the single-frequency signal is the result of subtracting the predicted received frequency from the received frequency. The received frequency is reconstructed and calibrated for the propagation delay in transiting the Earth's troposphere and ionosphere. The prediction model used by the

MaRS team has considered the accounts for gravitational forces of planetary gravity field and all other planets as third body attractions. Meanwhile, the non-gravitational forces like solar radiation pressure, the motion of Mars in its orbit, the motion and rotation of Earth, solid Earth tides, plate tectonics, the relativistic Doppler effect, and the finite light time between transmission and reception of radio signals were also included in the prediction (Pätzold et al., 2016). But there still exists bias in the data, such as orbit errors. Before the electron density retrieval, a step named baseline correction is usually used to calibrate the other error effects on the signals. Because the frequency residuals are considered to be zero at the upper atmosphere, we set the impact parameter of 3690 km as a boundary; linear fitting of the relationship between the frequency residuals and the impact parameter, computed from the 'raw' residuals higher than the boundary, is used to correct the biases. As an example, Figure 2 shows a comparison of frequency residuals before and after correction for the same occultation event for both X- and S-Band signals.

First of all, we can see that the S-Band signal has larger average amplitude and is much noisier than the X-Band signal; this is to be expected, given the frequency difference. Hereafter we will focus on the X-Band signal. After the baseline correction, the frequency residual profile is stable and its value at the higher impact parameter is almost 0, which implies that the baseline correction is contributing. In addition, we also found that there exist nonlinear variations of frequency residuals versus impact parameter because of the nonlinear orbital perturbation in some occultation events. For these events, the linear fitting baseline correction does not work well, so we use a quadratic fitting correction. Figure 3 shows two such examples, which compare the impact parameter variation of the frequency residuals between the linear and quadratic correction. As can be seen, for these two cases, quadratic correction could generate more reasonable profiles. Quadratic correction is used in a total of 10 of the 641 events that we process here.

For a radio signal passing through the Martian atmosphere, the relationship between the bending angle and the frequency residual is given as follows (Fjeldbo et al., 1971):

$$\begin{aligned}\Delta f =&\left[f - f\frac{V_{\mathrm{C}\_r}}{c}\cos(\phi_1-\phi_2) - f\frac{V_{\mathrm{C}\_z}}{c}\sin(\phi_1-\phi_2)\right.\\&\left.+ f\frac{V_{\mathrm{E}\_z}}{c}\cos(\varphi_1-\varphi_2) + f\frac{V_{\mathrm{E}\_r}}{c}\sin(\varphi_1-\varphi_2)\right]\\&-\left[f - f\frac{V_{\mathrm{C}\_r}}{c}\cos(\phi_1) - f\frac{V_{\mathrm{C}\_z}}{c}\sin(\phi_1)\right.\\&\left.+ f\frac{V_{\mathrm{E}\_z}}{c}\cos(\varphi_1) + f\frac{V_{\mathrm{E}\_r}}{c}\sin(\varphi_1)\right],\end{aligned}\tag{3}$$

in which, f is the carrier frequency of signal; c is the light velocity; $(V_{\mathrm{C}\_r}, V_{\mathrm{C}\_z})$ and $V_{\mathrm{E}\_r}, V_{\mathrm{E}\_z})$ are respectively the velocities of the spacecraft and of the Earth along the r, z axes in the occultation plane coordinate system, and the angles $\phi_1, \phi_2, \varphi_1, \varphi_2$ are defined in Figure 1. With the hypothesis of a spherically symmetric atmosphere, the impact parameter, defined as the distance from the center of Mars to the asymptote of the ray, is derived through the following formula:

$$a = \sqrt{r_{\mathrm{C}}^2 + z_{\mathrm{C}}^2}\sin(\phi_1 - \delta - \phi_2) = -z_{\mathrm{E}}\sin(\varphi_1 - \varphi_2).\tag{4}$$

This approach is valid only for spherically symmetric objects; occultation inversion at oblate objects, such as Jupiter or Saturn, is not applicable without modification (Withers et al., 2014; Pätzold et al., 2016). We replace ϕ_2, φ_2 with $\phi_2 + \Delta\phi_2, \varphi_2 + \Delta\varphi_2$ as Fjeldbo et al. (1971) did, and simplify the equations of (3) and (4) to:

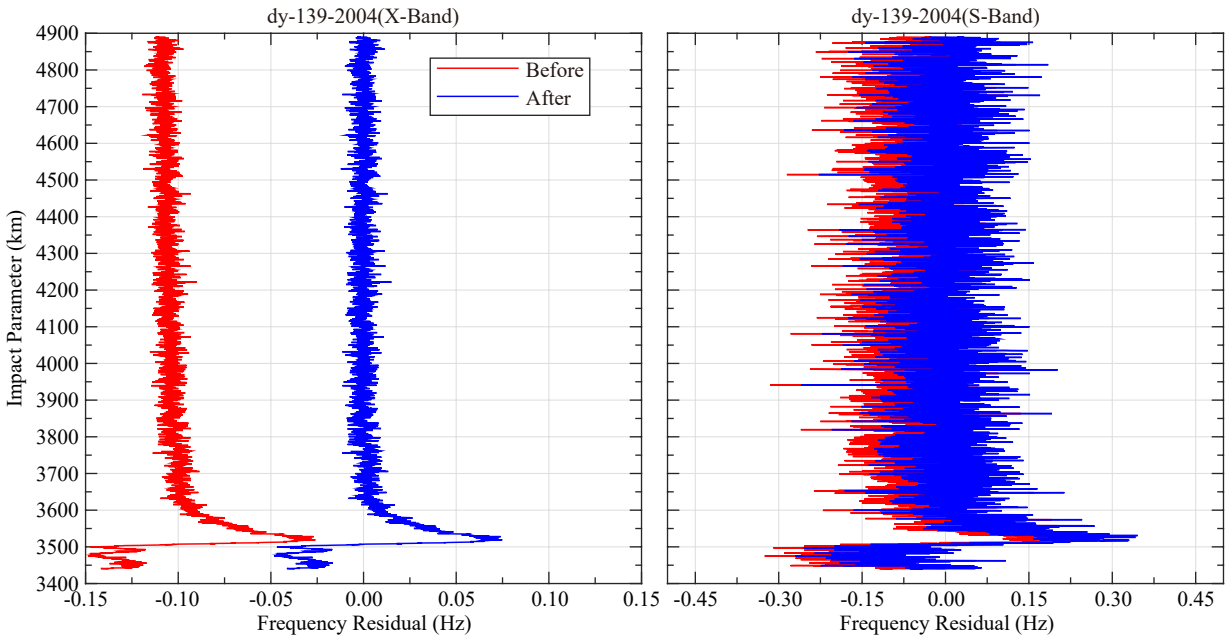

Figure 2. Example of frequency residuals variations (dy-139-2004) versus impact parameter before (red) and after (blue) the baseline correction for both X-(left) and S-(right) Band, respectively. The notation "dy-139-2004" gives the year and the day of year for the occultation event.

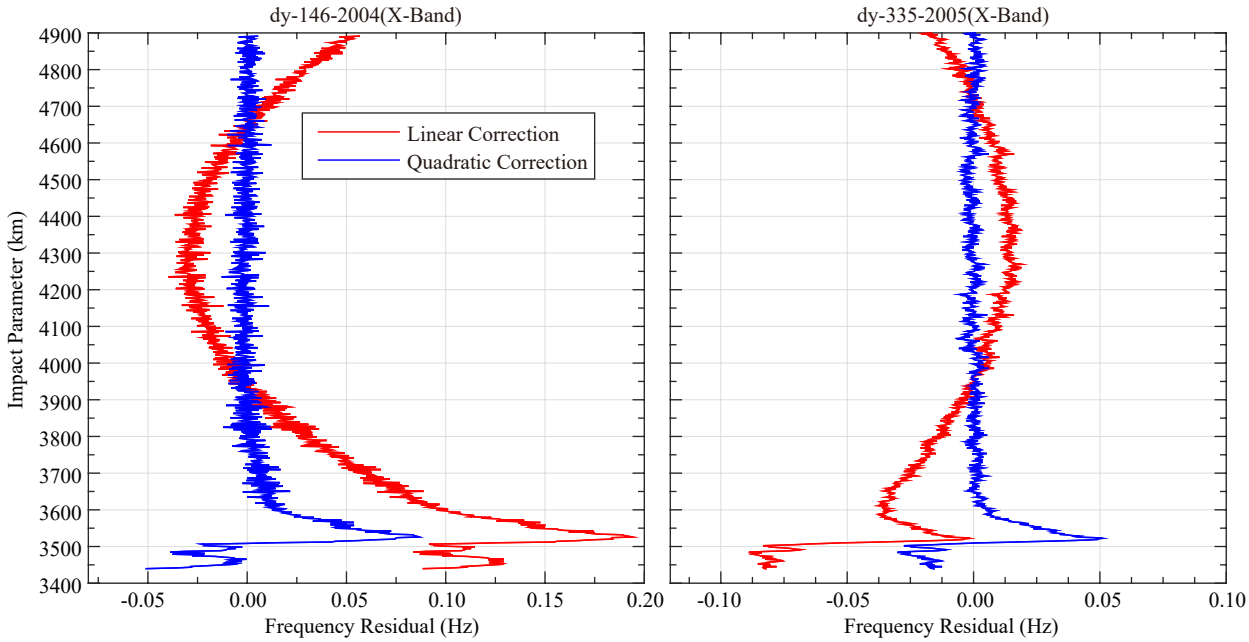

Figure 3. Two examples of frequency residuals variations versus impact parameter for linear (red) and quadratic (blue) correction, respectively.

$$\begin{cases} b_{11}\Delta\phi_2 + b_{12}\Delta\varphi_2 = k_1, \\ b_{21}\Delta\phi_2 + b_{22}\Delta\varphi_2 = k_2, \end{cases} \tag{5}$$

in which,

$$\begin{aligned} b_{11} &= V_{\mathrm{C}\_z}\cos(\phi_1-\phi_2) - V_{\mathrm{C}\_r}\sin(\phi_1-\phi_2), \\ b_{12} &= V_{\mathrm{E}\_z}\sin(\varphi_1-\varphi_2) - V_{\mathrm{E}\_r}\cos(\varphi_1-\varphi_2), \\ k_1 &= c\frac{\Delta f}{f} + V_{\mathrm{C}\_r}[\cos(\phi_1-\phi_2)-\cos(\phi_1)] \\ &\quad + V_{\mathrm{C}\_z}[\sin(\phi_1-\phi_2)-\sin(\phi_1)] \\ &\quad - V_{\mathrm{E}\_r}[\sin(\varphi_1-\varphi_2)-\sin(\varphi_1)] - V_{\mathrm{E}\_z}[\cos(\varphi_1-\varphi_2)-\cos(\varphi_1)], \\ b_{21} &= \sqrt{r_{\mathrm{C}}^2+z_{\mathrm{C}}^2}\cos(\phi_1-\delta-\phi_2), \\ b_{22} &= z_{\mathrm{E}}\cos(\varphi_1-\varphi_2), \\ k_2 &= z_{\mathrm{E}}\sin(\varphi_1-\varphi_2) + \sqrt{r_{\mathrm{C}}^2+z_{\mathrm{C}}^2}\sin(\phi_1-\delta-\phi_2). \end{aligned} \tag{6}$$

We start with rays passing through the upper altitude where both ϕ_2, φ_2 are almost zero and then proceed to the ray at lower altitudes step by step. For each ray, the initial estimates of ϕ_2, φ_2 are based on rays at higher altitudes and the corrections terms $\Delta\phi_2, \Delta\varphi_2$ are determined from equation (5). The new values of ϕ_2, φ_2 are then fed back into equation (5) for the next computation. The ray bending angle is computed as:

$$\alpha = \phi_2 + \varphi_2. \tag{7}$$

Given the ray bending angle α and the impact parameter a, the refractive index $\mu(r)$ versus the radial distance r, defined as the closest approach distance, is expressed by the Abel transformation (Healy, 2001):

$$\mu(r_i) = \exp\left(\frac{1}{\pi}\int_{a_i}^{\infty}\frac{\alpha(a)}{\sqrt{a^2-a_i^2}}\mathrm{d}a\right), \tag{8}$$

where the radial distance is $r_i = \dfrac{a}{\mu(r_i)}$ for the ith layer of ionosphere (Bouger's law). Meanwhile, in practice a numerical approximation is made for the integral of formula (8):

$$\mu(r_i) = \exp\left(\frac{1}{\pi}\sum_{k=i}^{m}\int_{a_k}^{a_{k+1}}\frac{\alpha(a)}{\sqrt{a^2-a_i^2}}\mathrm{d}a\right), \tag{9}$$

in which, m is the total layers of ionosphere. Since the bending at the upper atmosphere is insignificant and the maximum altitude when the radio signals passed atmosphere in MaRS is ~1500 km (Pätzold et al., 2005), the upper integral limit is set to be 4890 km in equation (9), considering that the mean radius of Mars is ~3390 km (Bullen, 1966). We assume that the bending angle varies linearly with the impact parameter in each single layer as expressed:

$$\alpha(a) = Aa + B, \tag{10}$$

among which, $A = \dfrac{\alpha(a_{k+1})-\alpha(a_k)}{a_{k+1}-a_k}$, $B = \dfrac{s_{k+1}\alpha(a_k)-s_k\alpha(a_{k+1})}{a_{k+1}-a_k}$. The approximate analytic solution of $\mu(r)$ from formula (9) is

$$\begin{aligned} \mu(r_i) = \exp\Bigg(\frac{1}{\pi}\sum_{k=i}^{n}\Bigg[A\left(\sqrt{a_{k+1}^2-a_i^2}-\sqrt{a_k^2-a_i^2}\right) \\ + B\ln\left|\frac{a_{k+1}+\sqrt{a_{k+1}^2-a_i^2})}{a_k+\sqrt{a_k^2-a_i^2}}\right|\Bigg]\Bigg). \end{aligned} \tag{11}$$

The term $\mu(r)-1$ is related to the electron density in the medium (Cahoy et al., 2006). The relationship between the refractivity and the electron density in the ionosphere can be expressed as:

$$[\mu(r)-1]\times 10^6 \approx -\kappa_{\mathrm{e}}N(r)\times 10^6, \tag{12}$$

where N is the electron density; $\kappa_{\mathrm{e}} \approx \dfrac{r_{\mathrm{e}}\lambda^2}{2\pi}$, λ is the signal wavelength; r_{e} is the classical electron radius, 2.8179×10^{-15} m. The EDPs are then retrieved from the observations based on the above algorithms. This method is appropriate to the single-fre-

quency data; for the differential Doppler of dual-frequency (X- and S-Band) observations, the retrieval is slightly different from the above algorithms.

In order to isolate the dispersive propagation effect of radio signals in the ionosphere, the differential Doppler is expressed as (Pätzold et al., 2016):

$$\Delta f_{\mathrm{S}}-\frac{3}{11}\Delta f_{\mathrm{X}}=\frac{40.32}{c}f_{\mathrm{S}}\left(\frac{1}{f_{\mathrm{S}}^2}-\frac{1}{f_{\mathrm{X}}^2}\right)\frac{\mathrm{d}}{\mathrm{d}t}\int_{\mathrm{C}}^{\mathrm{E}}N\mathrm{d}s, \tag{13}$$

in which, $f_{\mathrm{X}}, f_{\mathrm{S}}$ and $\Delta f_{\mathrm{X}}, \Delta f_{\mathrm{S}}$ are the carrier frequency and observed Doppler shifts of X- and S-Band, respectively, and s is the signal ray. For each ray, given the differential Doppler, the total electron content (TEC) along the ith ray is computed via:

$$(\mathrm{TEC}_{\mathrm{C-E}})_i=\sum_{k=1}^{i}\left\{\mathrm{d}t_i(\Delta f_{\mathrm{S}}-\frac{3}{11}\Delta f_{\mathrm{X}})_i\Big/\left[\frac{40.32}{c}f_{\mathrm{S}}\left(\frac{1}{f_{\mathrm{S}}^2}-\frac{1}{f_{\mathrm{X}}^2}\right)\right]\right\}, \tag{14}$$

where dt is the time interval of observation. The TEC is the integrated value of electron along the ray through:

$$\mathrm{TEC}_{\mathrm{C-E}}=\int_{\mathrm{C}}^{\mathrm{E}}N\mathrm{d}s=\int_{\mathrm{C}}^{\mathrm{E}}\frac{N(r)\times r}{\sqrt{r^2-a^2}}\mathrm{d}r, \tag{15}$$

where $a^2+s^2=r^2$, a is the impact parameter, and r is the radial distance. After the Abel transform, the electron density profiles can be obtained from formula (15), assuming a spherically symmetric ionosphere.

4. Parameter Optimization

The assumption of a linear relationship between the bending angle and the impact parameter in each single layer is the key factor for the approximate analytic solution of the refractive index. Either linear or quadratic fitting could be used in the processing. As an example, in Figure 4 we compare the retrieved electron density profiles between quadratic and linear fitting for the same occultation event with sampling frequency of 1Hz. The inversion results of electron density show the basic bimodal characteristics of the Martian ionosphere (Pätzold et al., 2005). The difference between the two profiles is given in the subplot. From the Figure, we can see that the difference between the two fittings is of the order of ~10^8 el/m^3, which is less than 1% of the peak electron density. To save computation time, the linear fitting is used hereafter in our processing.

For each occultation event there are two bands of observations (X-, and S-Band). Depending on the geometry of the spacecraft and Earth, the signal is tracked in either open-loop or close-loop mode. Figure 5 shows an example of the retrieved EDPs from single-frequency and dual-frequency differential Doppler with open-loop tracking mode for the same occultation event at

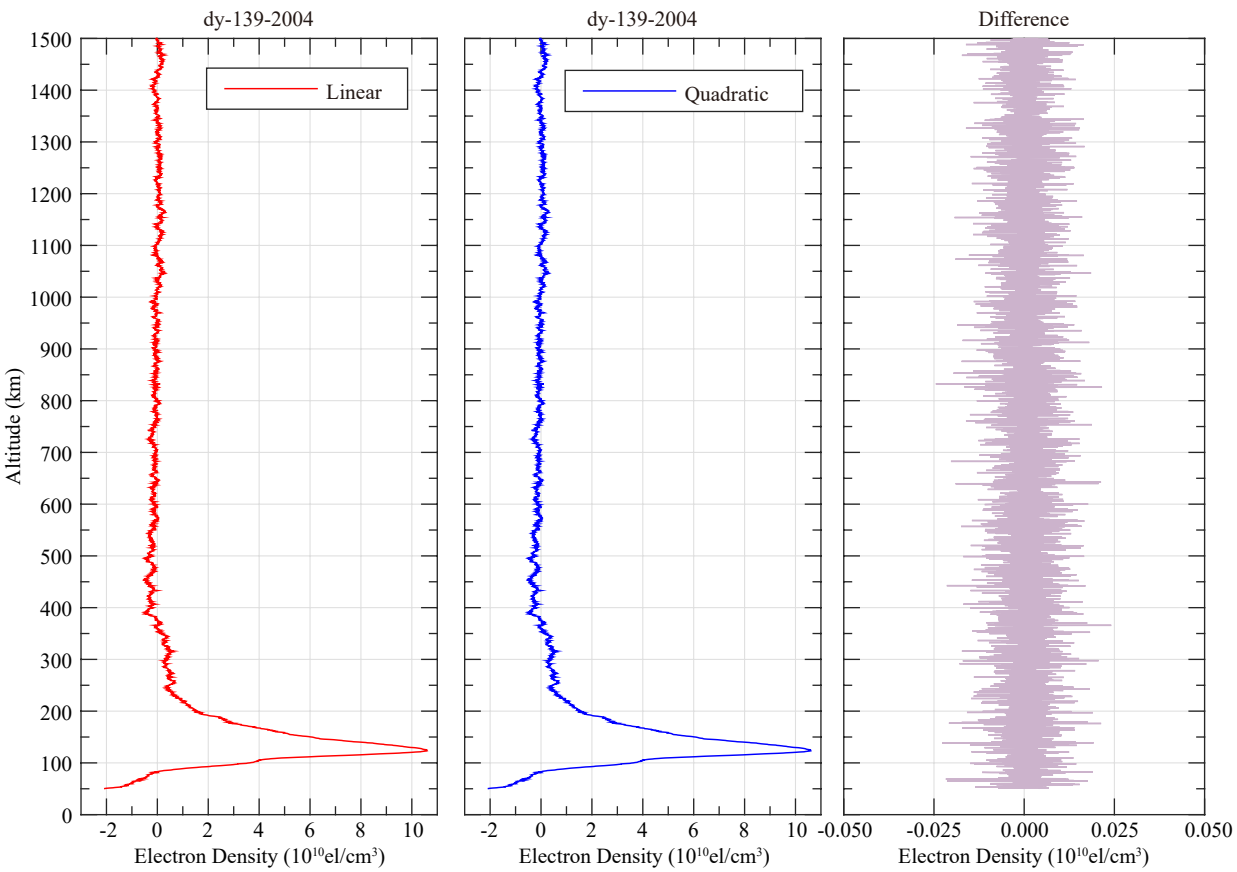

Figure 4. Left and Middle: Example of retrieved electron density profile variations versus altitude for linear (red) vs. quadratic (blue) assumption between bending and impact parameters in each single layer, respectively; Right: The difference between the two profiles.

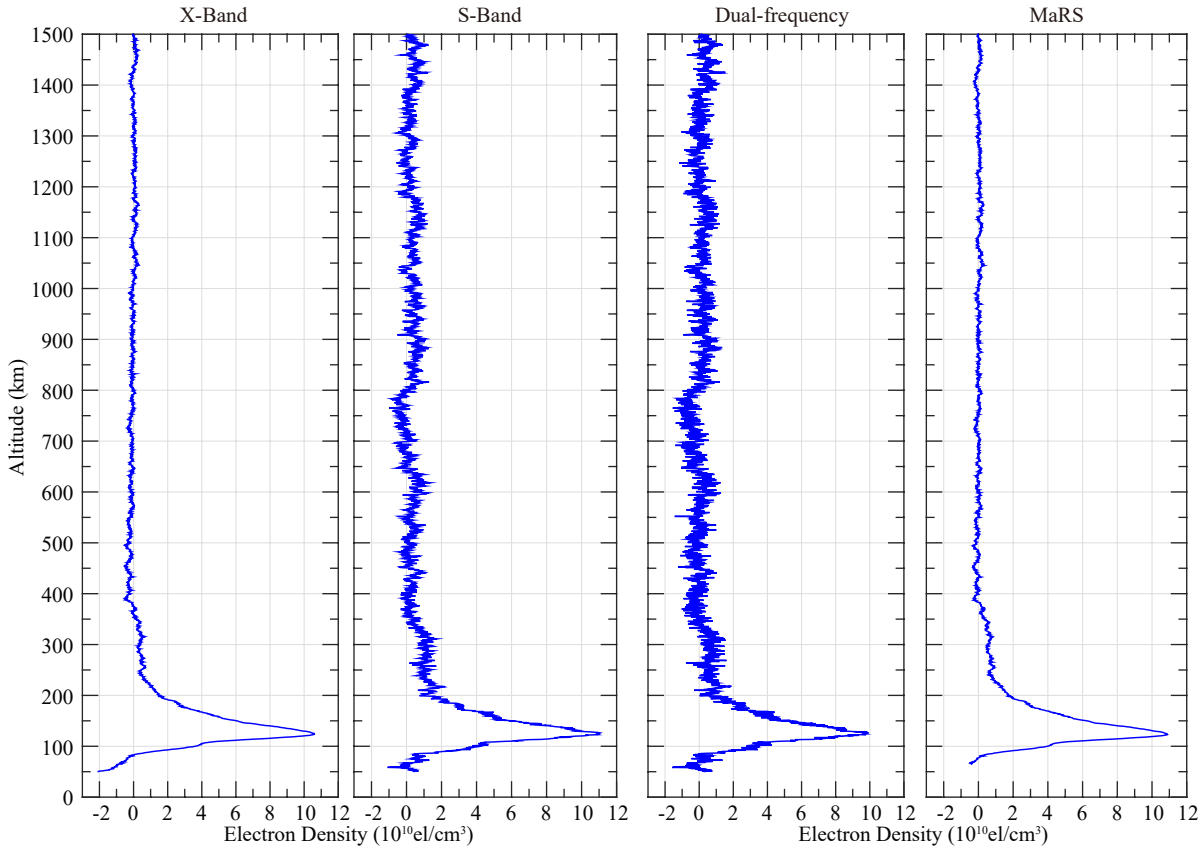

Figure 5. Comparison of the retrieved electron density profile variations versus altitude for single X-(first column), S-(second column) Band and dual-frequency differential Doppler (third column) with open-loop mode to the electron density profile published by MaRS (fourth column) for the same occultation event during 2004.05.18 (dy-139-2004).

2004.05.18 (dy-139-2004). The single S-Band frequency result is obviously noisier than that of the single X-Band frequency. The main features of the ionosphere are similar in both EDPs though the two profiles do exhibit minor differences. The peak electron density and altitude from X-Band and S-Band signals are respectively 10.595×10^{10} el/m^3, 123.4 km and 11.065×10^{10} el/m^3, 126.3 km while the results reported by the MARS team are 10.891×10^{10} el/m^3, 122.9 km (as published on http://pds-geosciences.wustl.edu/mex/mex-m-mrs-5-occ-v2.0/). During the processing, we prefer to use higher frequency signals if available. Additionally, we also presented the EDP from the dual-frequency differential Doppler in Figure 5 as a comparison. The main features of the ionosphere are similar and the difference is insignificant. But the dual-frequency results should be more reliable in the topside and lower area because non-ionospheric effects are eliminated. Figure 6 shows another example with different sampling frequency under close-loop tracking mode. It is apparent that the profile with higher sampling frequency has larger noise and oscillations.

During the baseline correction, the choice of boundary height might influence the final retrieval results. As an example, Figure 7 compares the EDPs with the baseline correction boundary at 3590 km, 3640 km and 3690 km for 3 typical occultation events. For convenience, we also show the difference of EDPs between 3590 km and 3690 km, and between 3640 km and 3690 km in the bottom panels. Overall, the amplitude of the difference with different baseline correction is ~1% of the peak density and the difference increases as the radial distance decreases. For the three cases shown here, the difference is either positive or negative, which might be due to the variations of realistic disturbance factors. In our processing, we finally choose 3690 km as the baseline correction boundary.

Another factor that might influence the retrieval result is the upper limitation in the integration of formula (8). As an example, Figure 8 compares the EDPs with 3890, 4390, and 4890 km upper limit for three typical occultation events. For convenience, in the bottom panels we also show the difference of EDPs between 3890 km and 4890 km upper limit, and between 4390 km and 4890 km upper limit. Overall, the amplitude of the difference with different upper limit integral height is ~1.5% of the peak density and could thus be considered negligible. In our processing, we finally choose 4890 km as the upper integral limit.

5. Independent Evaluation

To evaluate our processing, we also made comparison between our processed results and the samples profiles published by MaRS (http://pds-geosciences.wustl.edu/mex/mex-m-mrs-5-occ-v2.0/). There are a total of 10 occultation events identified that were processed by us successfully and published by the website as well. Figure 9 shows the mean difference and standard deviation of the EDPs between both retrievals versus altitude. The mean value of

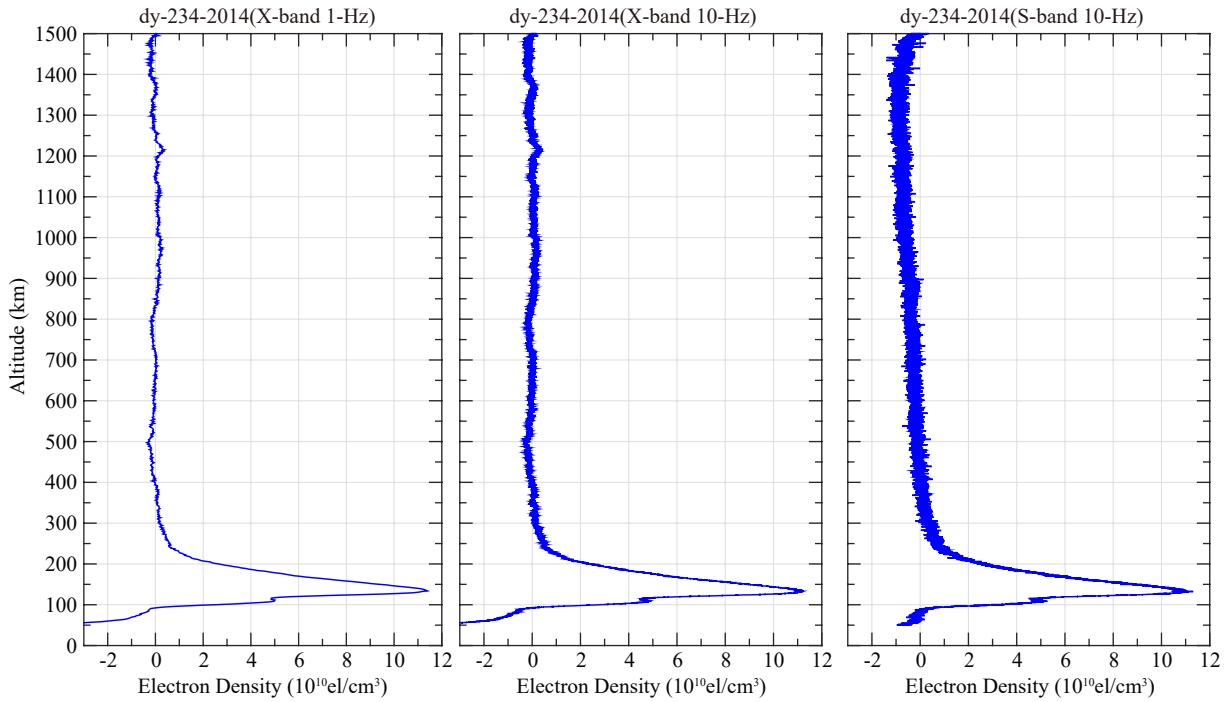

Figure 6. Example of retrieved electron density profile variations versus altitude for single X-Band 1-Hz sampling (left), X-Band 10-Hz sampling (middle) and S-Band 10-Hz sampling (right) signals with close-loop mode for the same occultation event of 2014.08.22 (dy-234-2014).

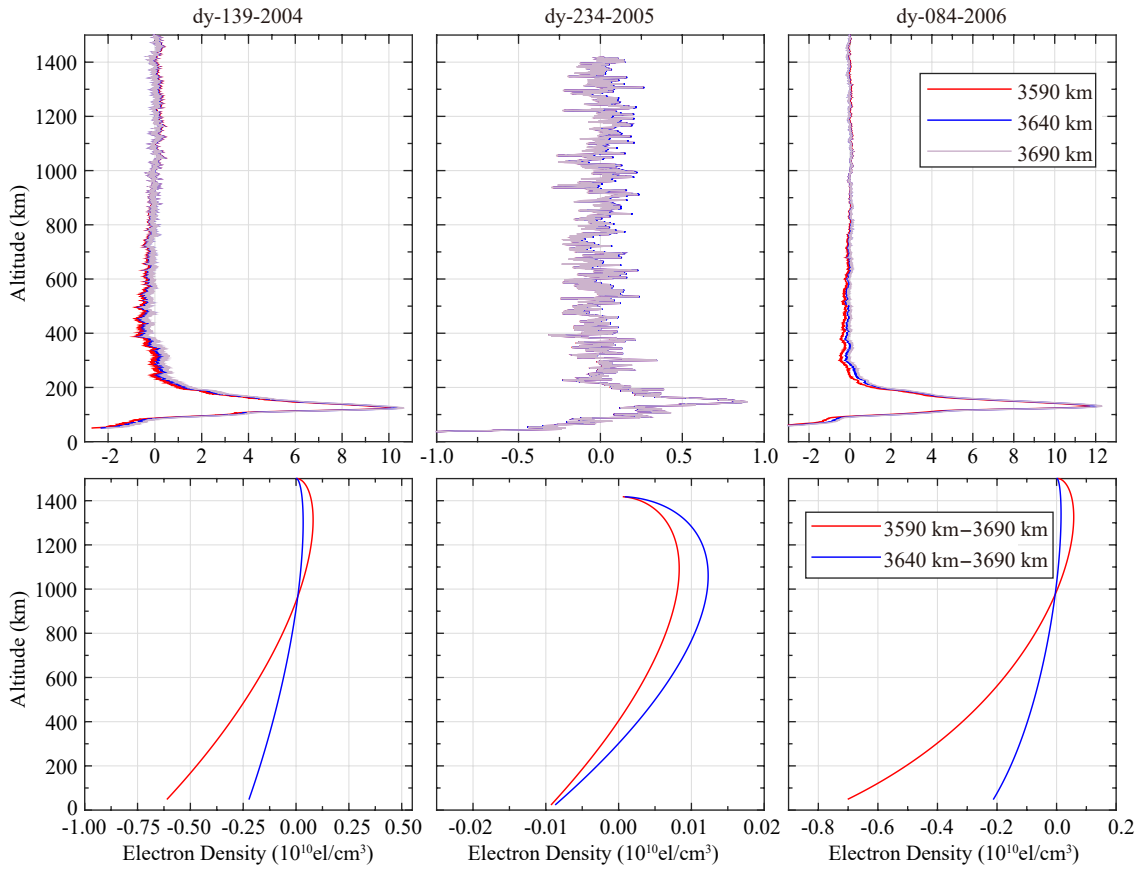

Figure 7. Top Panel: Examples of the electron density profile with 3590 km (red), 3640 km (blue) and 3690 km (purple) baseline correction boundary in the retrieval for three typical occultation events; Bottom Panel: The difference of electron density profiles between 3590 km and 3690 km (red), and between 3640 km and 3690 km (blue) baseline correction boundary choice.

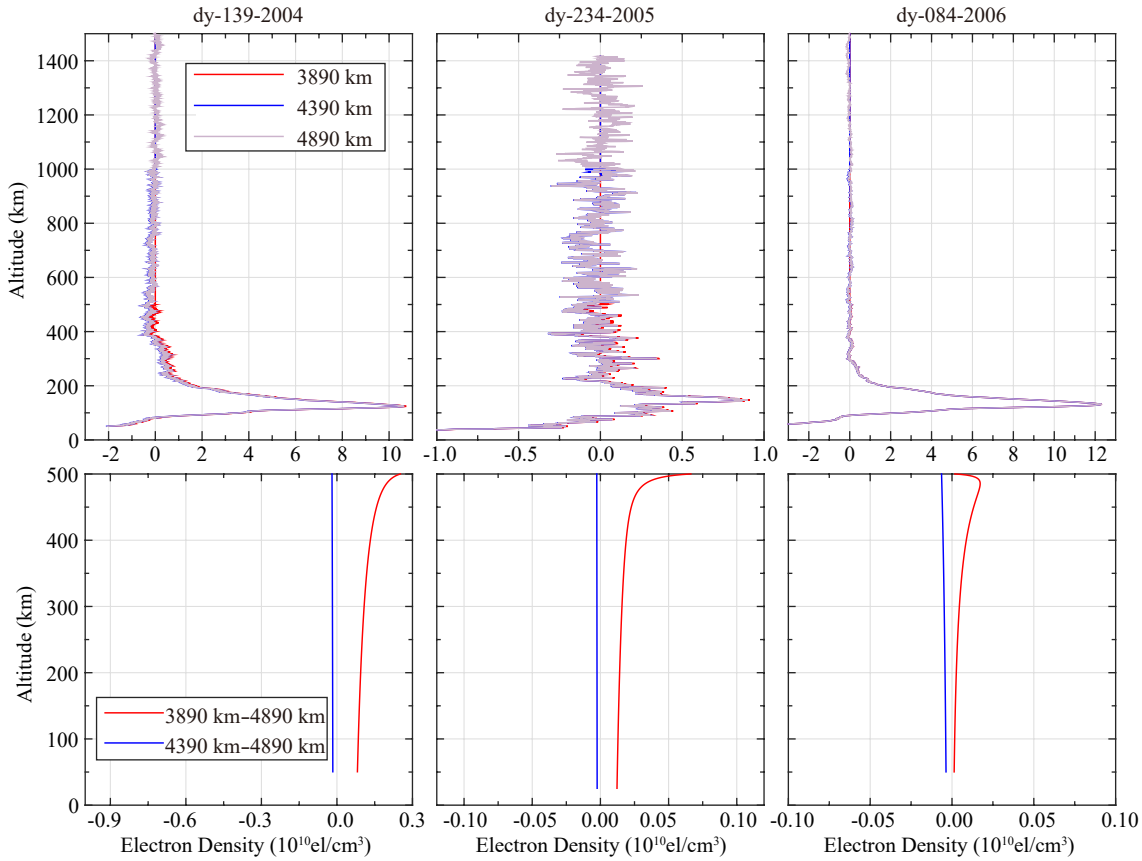

Figure 8. Top Panels: Examples of the electron density profile with 3890 km (red), 4390 km (blue), and 4890 km (purple) upper limit in the integration process of the retrieval for three typical occultation events; Bottom Panels: The difference of electron density profiles between 3890 km and 4890 km (red) upper limit, and between 4390 km and 4890 km (blue) upper limits.

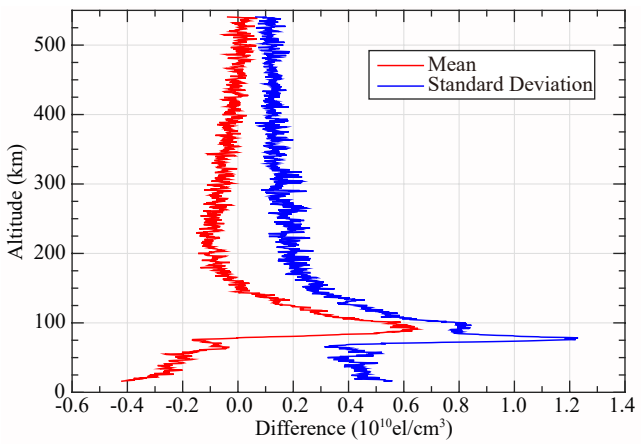

Figure 9. Mean (red) difference and standard deviation (blue) of the electron density profiles versus altitude between our results and the sample profiles published by MaRS.

the mean difference and standard deviation is 0.0127×10^{10} el/m^3 and 0.2535×10^{10} el/m^3, respectively. The mean difference and standard deviation of the peak electron density and peak altitude of the 10 profiles is 0.5322×10^{10} el/m^3, –0.5 km and 0.7561×10^{10} el/m^3, 4.0 km, respectively. The results are acceptable.

6. The Sporadic Layers of the Martian Ionosphere

Layers of metal ions produced by meteoroid ablation have been known in the Earth's ionosphere for decades (Withers et al., 2013); evidence for a similar layer in the Martian ionosphere, around 90 km, was first obtained from the MGS RS experiment (Fox, 2004). Then, 10 and 71 EDPs with this sporadic layer occurrence were identified in the early data of Mars Express and Mars Global Surveyor, respectively (Pätzold et al., 2005; Withers et al., 2008). The sporadic layers reported in this early research were not limited to specific times of day, or longitude or latitude in the Martian ionosphere, and no clear explanation of them was offered. Possible impact factors identified that could account for their occurrence included internal factors such as changes in neutral atmospheric dynamics and external factors such as the meteoroid influx rate. (Molina-Cuberos et al., 2003; Withers et al., 2013). Increasing data from investigations of the Martian ionosphere are providing a basis for further study of this layer.

When processing the EDPs, in some profiles we also find the sporadic layers below the two-layer structure, as shown in Figure 10. We went through all processed profiles manually, and obtained totally 24 profiles that display an obvious sporadic layer. From our statistical results, the peak altitude range of the sporadic layer is from 56 km to 94 km, where electron densities are from 0.08×10^{10} el/m^3 to 2.32×10^{10} el/m^3, and the mean value is about

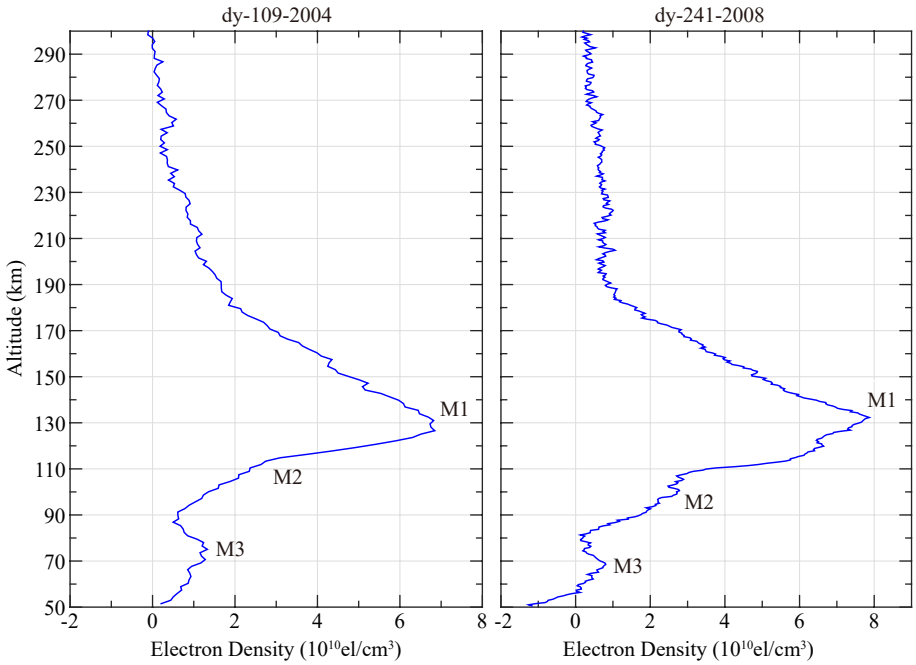

Figure 10. Two examples of retrieved electron density profile variations versus altitude (Mars mean radius=~3390 km) with obvious sporadic layer (M3) occurrence. The corresponding M1 and M2 layers are also marked in the subplot.

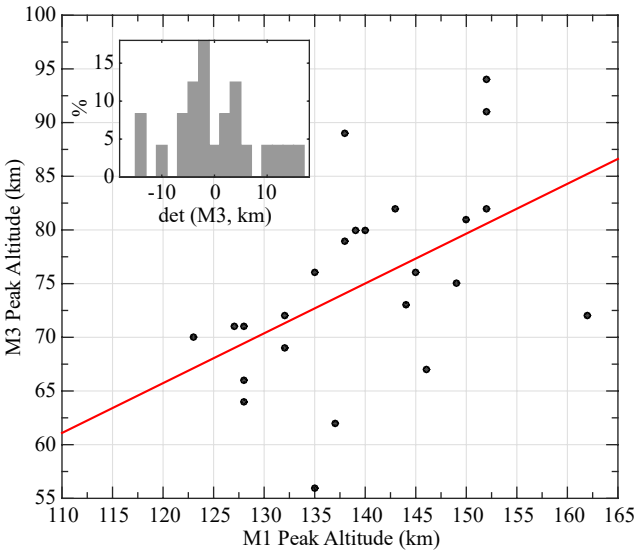

Figure 11. M3 (sporadic layer) peak altitudes versus M1 peak altitudes for the identified radio occultation cases with obvious sporadic layer occurrence. The red line is the corresponding least square fit result between two altitudes. The statistical result of the fitting residual was given in the embedded subplot.

0.65×10^{10} el/m^3. The dependence of its peak altitude on the main peak altitude is given in Figure 11. The results imply that the peak altitude is increasing with the main peak altitude, which is known to be related to the solar zenith angle (Zhang MHG et al., 1990; Bougher et al., 2004; Zou H et al., 2005, 2006, 2011; Withers, 2009). The successful identification of sporadic layer occurrence also confirms the high quality of our processing and parameters configuration.

7. Conclusion

In this paper, we have demonstrated the retrieval of the Martian ionospheric electron density profile using frequency residuals and differential Doppler from the MEX radio science experiment. About 640 profiles published from 2004 to 2015 of MEX have been processed. The optimized parameters including the boundary 3690 km for the baseline correction, the upper integral limit of 4890 km, and linear change of bending angle in the single layer versus impact parameter were used in the data processing. We then compared our results with the sample profiles published by MaRS, for 10 available occultation events. The mean value of the mean difference and standard deviation between both retrievals is 0.0127×10^{10} el/m^3 and 0.2535×10^{10} el/m^3, respectively. The mean difference and standard deviation of the peak electron density and peak altitude is 0.5322×10^{10} el/m^3, –0.5 km and 0.7561×10^{10} el/m^3, 4.0 km, respectively, which strongly suggests that our processing is reasonable and reliable. But if our hypothesis of a spherically symmetric atmosphere is found to be an oversimplification, our method should be modified.

We have identified manually 24 profiles with sporadic layer occurrence. The altitude of this layer ranges from 56 km to 94 km and its mean peak electron density is about 0.65×10^{10} el/m^3. Its peak altitude increases with the main peak altitude in the Martian ionosphere. And the main peak altitude is affected by the solar zenith angle.

Acknowledgment

XinAn Yue and Yong Wei gratefully acknowledge the support by the Thousand Young Talent Program of China. This work was also funded by the National Science Foundation of China (41661164034, 41525016). The MaRS data and SPICE Software

were accessed through http://pds-geosciences.wustl.edu/missions/mars_express/mars.htm, and https://naif.jpl.nasa.gov/naif/toolkit.html, respectively.

References

Bougher, S. W., Engel, S., Hinson, D. P., and Murphy, J. R. (2004). MGS Radio Science electron density profiles: Interannual variability and implications for the Martian neutral atmosphere. *J. Geophys. Res.*, *109*(E3), E03010. https://doi.org/10.1029/2003JE002154

Bullen, K. E. (1966). Implications of the revised mars radius. *Nature*, *211*(5047), 396. https://doi.org/10.1038/211396a0

Cahoy, K. L., Hinson, D. P., and Tyler, G. L. (2006). Radio science measurements of atmospheric refractivity with Mars Global Surveyor. *J. Geophys. Res.*, *111*(E5), E05003. https://doi.org/10.1029/2005JE002634

Chicarro, A., Martin, P., and Trautner, R. (2004). The Mars Express mission: an overview. Mars Express the Scientific Payload, 1240: 3–13. http://sci.esa.int/science-e/www/object/doc.cfm?fobjectid=35549

Fjeldbo, G., and Eshleman, V. R. (1965). The bistatic radar-occultation method for the study of planetary atmospheres. *J. Geophys. Res.*, *70*(13), 3217–3225. https://doi.org/10.1029/JZ070i013p03217

Fjeldbo, G., and Eshleman, V. R. (1969). Atmosphere of Venus as studied with the Mariner 5 dual radio-frequency occultation experiment. *Radio Sci.*, *4*(10), 879–897. https://doi.org/10.1029/RS004i010p00879

Fjeldbo, G., Kliore, A. J., and Seidel, B. (1970). The mariner 1969 occultation measurements of the upper atmosphere of Mars. *Radio Sci.*, *5*(2), 381–386. https://doi.org/10.1029/RS005i002p00381

Fjeldbo, G., Kliore, A. J., and Eshleman, V. R. (1971). The neutral atmosphere of Venus as studied with the Mariner V radio occultation experiments. *Astron. J.*, *76*, 123–140. https://doi.org/10.1086/111096

Fox, J. L. (2004). Advances in the aeronomy of Venus and Mars. *Adv. Space Res.*, *33*(2), 132–139. https://doi.org/10.1016/j.asr.2003.08.014

Grandin, M., Blelly, P., Witasse, O., and Marchaudon, A. (2015). Mars Express radio-occultation data: A novel analysis approach. *J. Geophys. Res.*:*Space Phys.*, *119*(12), 10621–10632. https://doi.org/10.1002/2014JA020698

Haider, S. A., and Mahajan, K. K. (2014). Lower and upper ionosphere of Mars. *Space Sci. Rev.*, *182*(1–4), 19–84. https://doi.org/10.1007/s11214-014-0058-2

Hantsch, M. H., and Bauer, S. J. (1990). Solar control of the Mars ionosphere. *Planet Space Sci.*, *38*(4), 539–542. https://doi.org/10.1016/0032-0633(90)90146-H

Healy, S. B. (2001). Radio occultation bending angle and impact parameter errors caused by horizontal refractive index gradients in the troposphere: A simulation study. *J. Geophys. Res.*, *106*(D11), 11875–11889. https://doi.org/10.1029/2001JD900050

Hinson, D. P., Simpson, R. A., Twicken, J. D., Tyler, G. L., and Flasar, F. M. (1999). Initial results from radio occultation measurements with Mars Global Surveyor. *J. Geophys. Res.*: *Planets*, *104*(E11), 26997–27012. https://doi.org/10.1029/1999JE001069

Jiang, X. Q., Yang, B., Li, S. (2018). Overview of China's 2020 Mars mission design and navigation. *Astrodynamics*, *2*(1), 1–11. https://doi.org/10.1007/s42064-017-0011-8

Kliore, A., Dan, L. C., Levy, G. S., Eshleman, V. R., Fjeldbo, G., and Drake, F. D. (1965). Occultation experiment: results of the first direct measurement of Mars's atmosphere and ionosphere. *Science*, *149*(3689), 1243–1248. https://doi.org/10.1126/science.149.3689.1243

Kliore, A. J., Cain, D. L., Fjeldbo, G., Seidel, B. L., and Rasoo, S. I. (1972). Mariner 9 S-Band Martian occultation experiment: initial results on the atmosphere and topography of Mars. *Science*, *175*(4019), 313–317. https://doi.org/10.1126/science.175.4019.313

Lindal, G. F., Hotz, H. B., Sweetnam, D. N., Shippony, Z., Brenkle, J. P., Hartsell, G. V., Spear, R. T., and Michael Jr, W. H. (1979). Viking radio occultation measurements of the atmosphere and topography of Mars: Data acquired during 1 Martian year of tracking. *J. Geophys. Res.*:*Solid Earth*, *84*(B14), 8443–8456. https://doi.org/10.1029/JB084iB14p08443

Marissa, F. V., Withers, P., Fallows, K., Flynn, C. L., Andrews, D. J., Duru, F., and Morgan, D. D. (2016). Electron densities in the ionosphere of Mars: A comparison of MARSIS and radio occultation measurements. *J. Geophys. Res.*:*Space Phys.*, *121*(10), 10241–10257. https://doi.org/10.1002/2016JA022987

Michael Jr, W. H., Cain, D. L., Fjeldbo, G., Davies, J. G., Grossi, M. D., Shapiro, I. I., and Tyler, G. L. (1972). Radio science experiments: The Viking Mars orbiter and Lander. *Icarus*, *16*(1), 57–73. https://doi.org/10.1016/0019-1035(72)90137-6

Molina-Cuberos, G. J., Witasse, O., Lebreton, J. P., Rodrigo, R.,and López-Moreno, J. J. (2003). Meteoric ions in the atmosphere of Mars. *Planet. Space Sci.*, *51*(3), 239–249. https://doi.org/10.1016/S0032-0633(02)00197-6

Pätzold, M., Neubauer, F. M., Carone, L., Hagermann, A., Stanzel1, C., Häusler, B., Remus, S., Selle, J., Hagl, D., … Dehant, V. (2004). MaRS: Mars express orbiter radio science. Mars Express the Scientific Payload, 1240: 141–163. http://sci.esa.int/science-e/www/object/doc.cfm?fobjectid=34889

Pätzold, M., Tellmann, S., Häusler, B., Hinson, D.,Schaa, R., and Tyler, G. L. (2005). A Sporadic Third Layer in the Ionosphere of Mars. *Science*, *310*(5749), 837–839. https://doi.org/10.1126/science.1117755

Pätzold, M., Tellmann, S., Andert, T., Carone, L., Fels, M., Schaa, R., Stanzel, C., Audenrieth-Kersten, I., Gahr, A., … Twicken, J. (2009). MaRS: Mars express radio science experiment. ESA SP-1291: 217–245. http://www.esa.int/esapub/sp/sp1240/sp1240web.pdf

Pätzold, M., Häusler, B., Tyler, G. L., Andert, T., Asmar, S. W., Bird, M. K., Dehant, V., Hinson, D. P., Rosenblatt, P., … Remus, S. (2016). Mars Express 10 years at Mars: Observations by the Mars Express Radio Science Experiment (MaRS). *Planet. Space Sci.*, *127*, 44–90. https://doi.org/10.1016/j.pss.2016.02.013

Peter, K., Pätzold, M., Molina-Cuberos, G., Witasse, O., González-Galindo, F., Withers, P., Bird, M. K., Häusler, B., Hinson, D. P., … Tyler, G. L. (2014). The dayside ionospheres of Mars and Venus: Comparing a one-dimensional photochemical model with MaRS (Mars Express) and VeRa (Venus Express) observations. *Icarus*, *233*, 66–82. https://doi.org/10.1016/j.icarus.2014.01.028

Sánchezcano, B., Witasse, O., Herraiz, M., Radicella, S. M., Bauer, J., Blelly, P. L., and Rodríguez-Caderot, G. (2012). Retrieval of ionospheric profiles from the Mars Express MARSIS experiment data and comparison with radiooccultation data. *Geosci. Instrum. Method Data Syst.*, *1*(1), 77–84. https://doi.org/10.5194/gi-1-77-2012

Withers, P., Mendillo, M., Hinson, D. P., and Cahoy, K. (2008). Physical characteristics and occurrence rates of meteoric plasma layers detected in the Martian ionosphere by the Mars Global Surveyor Radio Science Experiment. *J. Geophys. Res.*:*Space Phys.*, *113*(A12), A12314. https://doi.org/10.1029/2008JA013636

Withers, P., (2009). A review of observed variability in the dayside ionosphere of Mars. *Adv. Space Res.*, *44*(3), 277–307. https://doi.org/10.1016/j.asr.2009.04.027

Withers, P., Fillingim, M. O., Lillis, R. J., Häusler, B., Hinson, D. P., Tyler, G. L., Pätzold, M., Peter, K., Tellmann, S., and Witasse, O. (2012). Observations of the nightside ionosphere of Mars by the Mars Express Radio Science Experiment (MaRS). *J. Geophys. Res.*, *117*(A12), A12307. https://doi.org/10.1029/2012JA018185

Withers, P., Christou, A. A., and Vaubaillon, J. (2013). Meteoric ion layers in the ionospheres of Venus and Mars: Early observations and consideration of the role of meteor showers. *Adv. Space Res.*, *52*(7), 1207–1216. https://doi.org/10.1016/j.asr.2013.06.012

Withers, P., Moore, L., Cahoy, K., and Beerer, I. (2014). How to process radio occultation data: 1. From time series of frequency residuals to vertical profiles of atmospheric and ionospheric properties. *Planet. Space Sci.*, *101*, 77–88. https://doi.org/10.1016/j.pss.2014.06.011

Withers, P., Weiner, S., and Ferreri, N. R. (2015). Recovery and validation of Mars ionospheric electron density profiles from Mariner 9. *Earth Planets Space*, *67*, 194. https://doi.org/10.1186/s40623-015-0364-2

Zhang, M. H. G., Luhmann, J. G., and Kliore, A. J. (1990). An observational study of the nightside ionospheres of Mars and Venus with radio occultation methods. *J. Geophys. Res.*, *95*(A10), 17095–17102. https://doi.org/10.1029/JA095iA10p17095

Zhang, S. J., Ping, J. S., Han, T. T., Mao, X. F., and Hong, Z. J. (2011).

Implementation of the Earth-based planetary radio occultation inversion technique. *Sci. China Phys. Mech. Astron.*, *54*(7), 1359–1366. https://doi.org/10.1007/s11433-011-4247-7

Zhang, S. J., Cui, J., Guo, P., Li, J. L., Ping, J. S., Jian, N. C., and Zhang, K. F. (2015). Martian electron density profiles retrieved from Mars Express dual-frequency radio occultation measurements. *Adv. Space Res.*, *55*(9), 2177–2189. https://doi.org/10.1016/j.asr.2015.01.030

Zou, H., Wang, J. S., and Nielsen, E. (2005). Effect of the seasonal variations in the lower atmosphere on the altitude of the ionospheric main peak at Mars. *J. Geophys. Res.*: *Space Phys.*, *110*(A9), A09311. https://doi.org/10.1029/2004JA010963

Zou, H., Wang, J. S., and Nielsen, E. (2006). Reevaluating the relationship between the Martian ionospheric peak density and the solar radiation. *J. Geophys. Res.*: *Space Phys.*, *111*(A7), A07305. https://doi.org/10.1029/2005JA011580

Zou, H., Lillis, R. J., Wang, J. S., and Nielsen, E. (2011). Determination of seasonal variations in the Martian neutral atmosphere from observations of ionospheric peak height. *J. Geophys. Res.*: *Planets*, *116*(E9), E09004. https://doi.org/10.1029/2005JA011580

Zou, H., Ye, Y. G., Wang, J. S., Nielsen E., Cui J., and Wang X. D. (2016). A method to estimate the neutral atmospheric density near the ionospheric main peak of Mars. *J. Geophys. Res.*: *Space Phys.*, *121*(4), 3464–3475. https://doi.org/10.1002/2015JA022304